



Optics Letters

Multifunctional mid-infrared photonic switch using a MEMS-based tunable waveguide coupler

QIFENG QIAO,^{1,2,3} MAHMUT SAMI YAZICI,^{2,3}  BOWEI DONG,^{2,3}  XINMIAO LIU,^{1,2,3} CHENGKUO LEE,^{2,3,4}  AND GUANGYA ZHOU^{1,3,5}

¹Department of Mechanical Engineering, National University of Singapore, 117579 Singapore, Singapore

²Department of Electrical and Computer Engineering, National University of Singapore, 117583 Singapore, Singapore

³Center for Intelligent Sensors and MEMS (CISM), National University of Singapore, 117608 Singapore, Singapore

⁴e-mail: eelec@nus.edu.sg

⁵e-mail: mpezgy@nus.edu.sg

Received 11 June 2020; revised 28 August 2020; accepted 31 August 2020; posted 31 August 2020 (Doc. ID 400132); published 1 October 2020

We demonstrate a multifunctional photonic switch on silicon-on-insulator platform operating at the mid-infrared wavelength range (3.85–4.05 μm) using suspended waveguides with sub-wavelength cladding and a micro-electro-mechanical systems (MEMS) tunable waveguide coupler. Leveraging the flip-chip bonding technology, a top wafer acting as the electrode is assembled above the silicon-on-insulator wafer to enable the electrostatic actuation. Experimental characterizations for the functions of the proposed device include (1) an optical attenuator with 25 dB depth using DC voltage actuation, (2) a 1×2 optical switch with response time of 8.9 μs and -3 dB bandwidth up to 127 kHz using AC voltage actuation, and (3) an on-chip integrated light chopper with the comparable performance of a commercial rotating disc light chopper. © 2020 Optical Society of America

<https://doi.org/10.1364/OL.400132>

The mid-infrared (MIR) on-chip photonic integrated circuit (PIC) has attracted widespread interest due to its many potential applications, such as biological and chemical sensing, absorption spectroscopy, and free-space communications [1]. As the dominant platform in near-infrared (NIR) photonics, the silicon-on-insulator (SOI) platform remains popular in MIR photonics. Gas sensing applications based on Si photonics waveguides have been demonstrated [2–4]. To avoid the absorption caused by a buried oxide (BOX) layer, a Si suspended waveguide with the selective removal of the BOX layer in SOI has been widely adopted [2,5]. A demonstration of CO₂ absorption spectroscopy using suspended Si waveguides at wavelength of 4.26 μm with a loss of 3 dB/cm has been reported experimentally [2]. Leveraging the design of subwavelength grating (SWG) cladding, the suspended SWG waveguide with a propagation loss of 3.6 dB/cm was demonstrated in Ref. [6]. With the improved fabrication technique, the propagation loss was reduced to 0.82 dB/cm in work that followed [7]. This approach helps in improving the mechanical stability of the suspended Si membrane and facilitating its fabrication [6,7].

In recent years, there has been rapid growth in the library of waveguide-based devices on an SOI platform for MIR PICs [5]. However, the present active components are still inadequate. Recently, optical modulators in the MIR region on the SOI platform have been demonstrated, exploiting thermal-optic tuning [8] and free-carrier injection [9]. Though Si photonic switches using thermal-optic or free-carrier effects have been widely reported [10,11], the weak perturbation of the refractive index limits their efficiency and scale. The use of these designs, based on the Mach–Zehnder interferometer (MZI), multimode interference (MMI), or ring resonators, makes it hard to avoid the problems of non-negligible loss or narrow bandwidth. MEMS actuation for the displacement of photonic waveguide possesses the inherent advantage of efficient switching [12]. Out-of-plane electrostatic actuation is favorable for MEMS integration with PICs because of its compatibility and compact footprint. Some NIR photonic switch circuits using MEMS electrostatic actuation have been demonstrated with a high extinction ratio and large scale [13–16]. Previously, a double-layer waveguide design with broadband switch performance was reported [13], but it raised a high requirement for the fabrication processes. A more practical approach is to use a pre-stressed bending MEMS cantilever on an SOI platform to boost the tuning range of a pair of waveguide couplers [16]. However, the tuning range is still limited by the BOX layer thickness with the existence of the pull-in effect. Specifically, given a BOX layer thickness of 2 μm , the effective tuning displacement counting from the plane of the Si device layer can be estimated to be upward till around 1.6 μm [17]. Marching into MIR photonics, MEMS for PICs demand a larger tuning displacement due to the extension of the wavelength.

In this Letter, we report the multifunctional photonic switch with the MEMS actuation operating in the MIR wavelength range from 3.85 to 4.05 μm . The suspended SWG waveguide is chosen for our study because of its good compatibility with MEMS design and fabrication. The flip-chip bonding technology is adopted to enable a double-layer configuration with a large air gap for MEMS electrostatic actuation. In addition, the proposed double-layer configuration brings more flexibility

to the optical design. For example, the separated actuation for the consecutive waveguide [18] can be easily realized with the electrodes on the top wafer. The finite difference time domain (FDTD) and finite element method (FEM) simulations were carried out to optimize the optical and mechanical response of the device. We present the experimental results of three optical functions.

Figure 1 shows the schematic of the proposed device. It consists of two parts, namely, a top wafer (SiO_2 wafer) and a bottom wafer (SOI wafer). These two wafers are fabricated separately and assembled via flip-chip bonding technology. The optical waveguides are located at the bottom wafer, including suspended SWG waveguides, grating couplers, and a tunable waveguide coupler with a MEMS cantilever. To enable the movement of the MEMS cantilever, the double-side cladding of the suspended SWG waveguide is converted to single-side cladding in the region of the MEMS cantilever. There is only one side of SWG cladding along the waveguide attached to the MEMS cantilever [see Fig. 1(a) inset]. Beyond the region of the MEMS cantilever, the single-side cladding is converted back to double-side cladding for mechanical stability. In this way, the movability of the MEMS cantilever can be achieved without the interruption of the optical waveguides. On the top wafer, the gold pad is patterned to cover the MEMS cantilever region. The aluminum solders, acting as the spacers and electrical interconnections, are prepared on both the top and bottom wafers for the flip-chip bonding. The details of the flip-chip bonding process were discussed in our previous work [19]. Since the aluminum solders work as the electrical interconnections between the two wafers, the voltage can be applied to the top wafer from the isolated gold pad on the SOI wafer. The silicon substrate is grounded to avoid any floating voltage. With the assembly of these two wafers, we can actuate the MEMS cantilever electrostatically by applying voltage between the top wafer and the Si device layer. As shown in Fig. 1(b), in the absence of voltage bias, the light propagating in the input suspended SWG waveguide is effectively coupled from input-port to drop-port after passing the waveguide coupler. During the through-state [Fig. 1(c)], a bias voltage is applied to bend the MEMS cantilever upwards, thus eliminating the light coupling between these two waveguides. Between the drop-state and through-state, the power-splitting ratio of the tunable waveguide coupler can be continuously modulated from 0 to 100% with electrostatic actuation. In this way, the proposed functions can be achieved.

In the first step, the optical designs on the SOI wafer, including the single-mode suspended SWG waveguide and the suspended waveguide coupler, were investigated. All devices in this study were designed for transverse electric (TE) polarization. We utilized an SOI wafer with a $0.5\ \mu\text{m}$ thick silicon device layer and a $2\ \mu\text{m}$ thick BOX layer. The basic structure of our waveguide design is illustrated in Fig. 2(a). The dimensions were the width of waveguide core $W_{\text{wg}} = 1.4\ \mu\text{m}$, the width of SWG cladding $W_{\text{clad}} = 4\ \mu\text{m}$, the silicon strip length $l_{\text{si}} = 0.2\ \mu\text{m}$, the air gap length $l_{\text{air}} = 0.4\ \mu\text{m}$, and the periodicity $\Lambda = 0.6\ \mu\text{m}$. With such an SWG cladding design, the Bragg reflection can be avoided and sufficient mechanical support can be offered. Next, we designed the waveguide coupler with Lumerical MODE software. Based on the effective medium theory, the SWG cladding was constructed as a uniform cladding in the simulation model [Fig. 2(b)]. Its equivalent refractive index n_{clad} can be given as 2.14 [20]. For the design of the waveguide coupler,

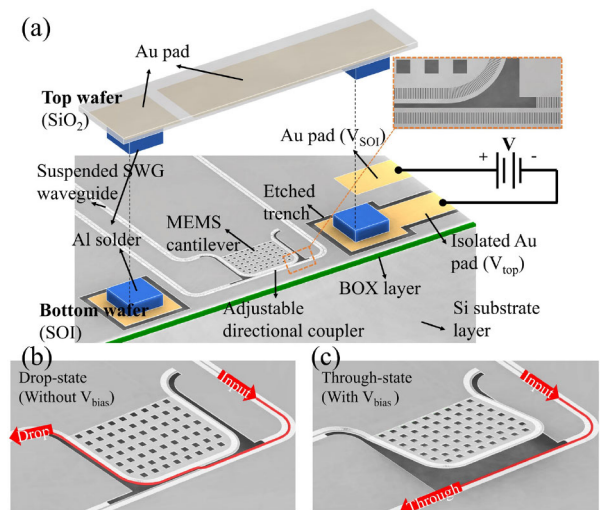


Fig. 1. Schematics of the proposed device. (a) Illustration of the operation mechanism. (b) Drop-state of the waveguide coupler. (c) Through-state of the waveguide coupler (actuated state).

$L_{\pi}(\lambda)$ dominates the device performance, which is defined as the coupling length required for a complete power transfer from one waveguide to the other. Considering our fabrication constraints, the coupling gap was set as $200\ \text{nm}$. Based on the simulation results [Fig. 2(c)], we selected a coupling length of $60\ \mu\text{m}$. Considering the mechanical stability of the suspended structure in SOI, the cantilever length was set as $85\ \mu\text{m}$. The waveguide structures were transferred to the Si device layer via E-beam lithography and deep reactive ion etching. Details about the fabrication process can be found in our previous work [19]. Then, diluted hydrofluoric (HF) acid was used to remove the BOX layer below the thoroughly etched Si waveguide device layer. For the top SiO_2 wafer, the patterned electric layout was achieved by optical lithography (LaserWriter LW405), following thermal evaporation ($5/80\ \text{nm}\ \text{Cr}/\text{Au}$) and a lift-off process. As shown in Fig. 3(a), the gold pads were prepared for the flip-chip bonding and the grating couplers were placed out of the bonding region. Thus, the fiber-chip light transmission could still be achieved after bonding. The surface coupling efficiency of the grating coupler was optimized with refractive index engineering [21] of the uniform SWGs to operate among the proposed working wavelength range. We used the cut-back method to investigate the propagation loss of the suspended SWG waveguide. The experimental setup has been discussed in our previous study [19]. The optical transmission was tested through straight waveguides with various lengths ranging from 0.032 to $3.032\ \text{cm}$. The propagation loss is $3.9 \pm 0.5\ \text{dB}/\text{cm}$ in the proposed working wavelength range, which is comparable to the propagation loss reported in Ref. [6]. With the proper design of the waveguide geometry, optical mode can be well confined in the waveguide core thereby reducing the leakage loss to the Si substrate. The propagation loss can be mainly attributed to the scattering loss caused by the roughness of the surface and the surrounding SWG cladding [22]. To further reduce the scattering loss, some improvements in the fabrication technology (e.g., reducing E-beam lithography spot size [7]), thermal oxidation [6] can be carried out. The flip chip bonding process was optimized to achieve a well-controlled gap around $15\ \mu\text{m}$ with sub-micron accuracy.

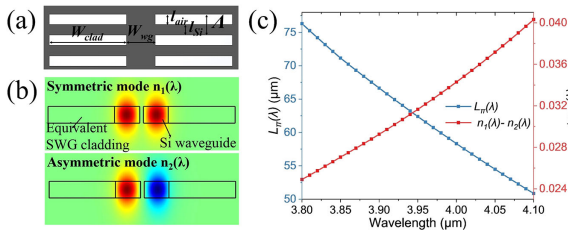


Fig. 2. (a) Waveguide with SWG cladding. (b) Mode profiles of the waveguide coupler. (c) L_π and Δn_{eff} versus wavelength.

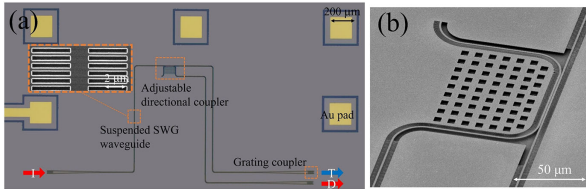


Fig. 3. (a) Optical design on the SOI wafer under optical microscope. (b) SEM image of the suspended waveguide coupler.

The scanning electronic microscope (SEM) image of the tunable waveguide coupler is shown in Fig. 3(b). A Thorlab photodetector PDAVJ5 (1 MHz bandwidth) was utilized. Due to the limited bandwidth of the grating coupler, we can only measure the wavelength range from 3.85 μm to 4.05 μm . It is shown in Fig. 4(a) that the measured results of the 60 μm coupling length design agreed well with the simulation results of a coupling length of 66 μm due to the extra coupling induced by the waveguide bending near the coupling region and fabrication imperfections. The insertion loss of the tunable waveguide coupler ((Drop + Through)/Input) was calculated to be -0.68 ± 0.22 dB. The optical transmission through a reference waveguide only was measured as the input transmission. The insertion loss can be well controlled owing to the good mode match at the interface of the mode conversion [Fig. 1(a) inset]. According to the simulation by Lumerical MODE, mode overlap can reach 98.3% at the interface of conversion. The measurements around wavelength 3.9 μm were flat because these points were below the detection limit of our photodetector. It can be found from Fig. 4(a) that the -20 dB bandwidth of the waveguide coupler is 100 nm. Dispersive engineering for a wavelength-flattened waveguide coupler [23] and broadband switch unit design [24] can be potentially utilized to further extend the operation bandwidth.

Next, we moved to the characterization of the proposed optical functions. First, we characterized the use of the device as an optical attenuator with quasi-static operation. The attenuation of drop-port operating at wavelength of 3.9 μm is shown in Fig. 4(b). The attenuation depth 25 dB can be achieved with 90 V applied. The attenuation of transmission was normalized to the drop-state transmission.

Second, we characterized the use of the device as a 1×2 optical switch with AC voltage actuation. Based on the waveguide coupler, optical transmission can be switched from drop-port to through-port with the electrostatic actuation of a MEMS cantilever. The optical transmission was normalized to the drop-state transmission. An AC square-wave voltage actuation having an amplitude of 90 V was applied to the device

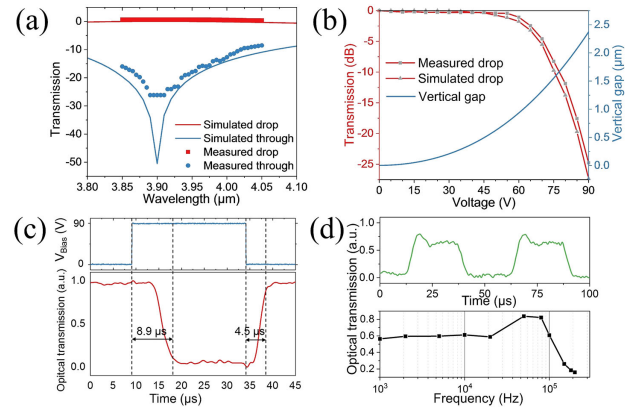


Fig. 4. (a) Transmission in the waveguide coupler. (b) Attenuation of drop port. (c) Response time of the optical switch. (d) Step response and frequency response of the MEMS cantilever.

with a frequency of 20 kHz. The falling time (to 10% power) and rising time (to 90% power) was 8.9 μs and 4.5 μs , respectively. The overshoot of the optical signal in response to the electrostatic actuation was not obvious, possibly due to the large displacement during vibration and air damping. It can be found in Fig. 4(b) that the optical transmission was much attenuated (-25 dB) at the through-state with the bias voltage 90 V. Thus, the through-state of the photonic switch was stable during the AC actuation. As there is no voltage applied, the returning of the MEMS cantilever to drop state was also stable because of the elastic behavior of Si MEMS. To investigate the mechanical frequency response of the MEMS cantilever, we applied a constant bias voltage 60 V and a small square-wave AC voltage with frequency scanning from 1 kHz to 200 kHz. The step response with the 20 kHz applied AC voltage is shown in the upper half of Fig. 4(d). The overshoot was visible due to the slight underdamping condition of the cantilever vibration. It can be found in Fig. 4(d) that the resonance frequency of the MEMS cantilever was around 70 kHz and the -3 dB bandwidth of AC actuation was up to 127 kHz.

Third, we characterized the use of the device as an on-chip light chopper with AC voltage actuation. The lock-in amplifier is a common approach for MIR device testing to improve signal-to-noise ratio [19]. In such an experimental setup, a photodetector and a rotating disk (RD) light chopper are usually utilized as the input signal and the reference signal, respectively, in the lock-in amplifier system [shown in Fig. 5(a)]. During the lock-in measurement, only the input signal oscillating at the reference frequency is sampled to enhanced signal to noise ratio. Moreover, it is demanded that the phase difference between the input and reference must be stable. The MIR laser was fixed at the wavelength of 3.9 μm during the following measurements. It is shown in Fig. 5(c) that the stability of the phase difference can be improved with the increased reference frequency from the RD light chopper. Next, we replaced the RD chopper with our on-chip PIC chopper. The experimental setup is shown in Fig. 5(b). We applied a constant bias voltage about 60 V and a square-wave AC voltage with a frequency of 100 Hz and an amplitude of 20 V to our on-chip device. At the same time, the square-wave AC voltage was sent to the lock-in amplifier as the reference signal. In such an experimental setup, as shown in Fig. 5(b), the proposed device vibrating under an applied AC

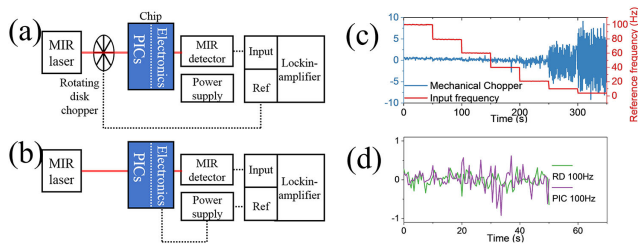


Fig. 5. (a) Simplified schematic for MIR photonic testing setup. (b) Modified setup for on-chip chopper. (c) Measurements of phase difference in lock-in amplifier under RD chopper testing. (d) Comparison between the RD and PIC chopper.

voltage serves as the light chopper. From the comparison of phase difference fluctuations in Fig. 5(d), it can be found that it is promising to integrate the light chopper function into the PIC chip using the proposed device.

Overall, the proposed photonic switch with an extinction ratio of 25 dB and an insertion loss of 0.68 dB shows a satisfactory performance. Due to the scaling up of mechanical and optical design with increasing wavelength, the time response of the proposed MIR optical switch ($8.9 \mu\text{s}$) is increased compared to the MEMS cantilever-based optical switch (falling time of $3.8 \mu\text{s}$) reported in NIR photonics [16]. In terms of performance, there are few reported MEMS photonics switches with an extinction ratio above 25 dB and an insertion loss below 1 dB in the literature [12]. Leveraging the SWG cladding design, the optical waveguide can be well integrated with the MEMS actuator, thereby achieving a low insertion loss. The large extinction ratio is due to the large actuation gap created by the flip-chip bonding. Considering the increasing scale of PICs and electronics, the air gap between the double-layer configuration should be narrowed to reduce the power consumption. To apply the proposed double-layer configuration on a large scale of PIC design, the flip-chip bonding process should be further optimized to achieve a precisely controlled air gap. Besides the bonding temperature and force, the designs for bonding solder should be carefully considered for the double-layer configuration, such as amount, location, material, thickness, and flatness. As single crystal silicon has a great potential resistance against aging [25], the proposed MEMS structure on SOI technology should have a promising working consistency. Further investigations on the MEMS actuator are needed to estimate the optical switch performance over a working lifetime.

In conclusion, we experimentally demonstrated three optical functions using the proposed MEMS-based photonic switch in the MIR wavelength range from 3.85 to $4.05 \mu\text{m}$. First, the optical attenuation can be achieved at a depth of 25 dB at wavelength $3.9 \mu\text{m}$ with 90 V DC voltage applied. Second, the optical switch was demonstrated with a response time of $8.9 \mu\text{s}$. The -3 dB bandwidth of the MEMS cantilever AC actuation can be up to 127 kHz. Third, it was demonstrated that the working performance of the proposed device as an on-chip light chopper is comparable to a commercial rotating disk light chopper. This work brings a valuable active functional component to the library of fundamental building blocks in MIR PICs.

Funding. Agency for Science, Technology and Research (R-263-000-C91-305); National Research Foundation Singapore (R-263-000-C24-281, R-263-000-C64-281).

Acknowledgment. We thank Prof. Aaron Thean and Dr. Yida Li for access to and training on the flip-chip bonding process.

Disclosures. The authors declare no conflicts of interest.

REFERENCES

- R. Soref, *Nat. Photonics* **4**, 495 (2010).
- F. Ottonello-Briano, C. Errando-Herranz, H. Rödjegård, H. Martin, H. Sohlström, and K. B. Gylfason, *Opt. Lett.* **45**, 109 (2019).
- C. Ranacher, C. Consani, A. Tortschanoff, R. Jannesari, M. Bergmeister, T. Grille, and B. Jakoby, *Sens. Actuators A Phys.* **277**, 117 (2018).
- C. Ranacher, C. Consani, N. Vollert, A. Tortschanoff, M. Bergmeister, T. Grille, and B. Jakoby, *IEEE Photon. J.* **10**, 2700614 (2018).
- Y. Zou, S. Chakravarty, C.-J. Chung, X. Xu, and R. T. Chen, *Photon. Res.* **6**, 254 (2018).
- J. S. Penadés, C. Alonso-Ramos, A. Khokhar, M. Nedeljkovic, L. Boodhoo, A. Ortega-Moñux, I. Molina-Fernández, P. Cheben, and G. Mashanovich, *Opt. Lett.* **39**, 5661 (2014).
- J. S. Penadés, A. Ortega-Monux, M. Nedeljkovic, J. G. Wanguemert-Perez, R. Halir, A. Z. Khokhar, C. Alonso-Ramos, Z. Qu, I. Molina-Fernandez, P. Cheben, and G. Z. Mashanovich, *Opt. Express* **24**, 22908 (2016).
- M. Nedeljkovic, S. Stanković, C. J. Mitchell, A. Z. Khokhar, S. A. Reynolds, D. J. Thomson, F. Y. Gardes, C. G. Littlejohns, G. T. Reed, and G. Z. Mashanovich, *IEEE Photon. Technol. Lett.* **26**, 1352 (2014).
- M. Nedeljkovic, C. G. Littlejohns, A. Z. Khokhar, M. Banakar, W. Cao, J. S. Penades, D. T. Tran, F. Y. Gardes, D. J. Thomson, G. T. Reed, H. Wang, and G. Z. Mashanovich, *Opt. Lett.* **44**, 915 (2019).
- R. A. Soref, F. De Leonardi, and V. M. N. Passaro, *J. Lightwave Technol.* **36**, 5254 (2018).
- S. Wei, W. Jian, L. Zhao, R. Zhang, J. Qiu, Z. Yin, and Y. Tian, in *Conference on Lasers and Electro-Optics (CLEO)-Laser Science to Photonic Applications* (Optical Society of America, 2014), paper JW2A.38.
- C. Errando-Herranz, A. Y. Takabayashi, P. Edinger, H. Sattari, K. B. Gylfason, and N. Quack, *IEEE J. Sel. Top. Quantum Electron.* **26**, 8200916 (2020).
- T. J. Seok, N. Quack, S. Han, R. S. Muller, and M. C. Wu, *Optica* **3**, 64 (2016).
- C. Lee and J.-L. A. Yeh, *J. Micro/Nano. MEMS MOEMS* **7**, 021003 (2008).
- C. Lee, *J. Lightwave Technol.* **25**, 490 (2007).
- S. Han, T. J. Seok, N. Quack, B.-W. Yoo, and M. C. Wu, *Optica* **2**, 370 (2015).
- G. O'Brien, D. J. Monk, and L. Lin, *Proc. SPIE* **4593**, 31 (2001).
- L. Li, C. Peng, Y. Qi, G. Zhou, Q. Qiao, F. S. Chau, and G. Zhou, *Opt. Express* **26**, 30362 (2018).
- M. S. Yazici, B. Dong, D. Hasan, F. Sun, and C. Lee, *Opt. Express* **28**, 11524 (2020).
- W. Zhou, Z. Cheng, X. Wu, X. Sun, and H. K. Tsang, *J. Appl. Phys.* **123**, 063103 (2018).
- N. Chen, B. Dong, X. Luo, H. Wang, N. Singh, G.-Q. Lo, and C. Lee, *Opt. Express* **26**, 26242 (2018).
- D. M. Kita, J. Michon, S. G. Johnson, and J. Hu, *Optica* **5**, 1046 (2018).
- B. Dong, X. Luo, T. Hu, T. X. Guo, H. Wang, D.-L. Kwong, P. G.-Q. Lo, and C. Lee, *IEEE J. Sel. Top. Quantum Electron.* **24**, 4500108 (2018).
- J. Van Campenhout, W. M. Green, S. Assefa, and Y. A. Vlasov, *Opt. Express* **17**, 24020 (2009).
- A. Neels, G. Bourban, H. Shea, A. Schifferle, E. Mazza, and A. Dommann, *Proc. Chem.* **1**, 820 (2009).